



Cite this: *Chem. Commun.*, 2024, 60, 3547

Received 9th January 2024,
Accepted 24th February 2024

DOI: 10.1039/d4cc00119b

rsc.li/chemcomm

Small-size and well-dispersed Fe nanoparticles embedded in carbon rods for efficient oxygen reduction reaction†

Xinde Duan, Fayuan Ge, Yang Liu and Hegen Zheng *

The preparation of ultra-small and well-dispersed metal nanoparticles (NPs) is of great importance for promoting oxygen reduction. Here, a metal (Fe and Zn) NP (7 nm) based catalyst derived from a Zn-based metal–organic framework was obtained by a vapor adsorption strategy, demonstrating a high half-wave potential (0.868 V) and power density (196 mW cm^{−2}).

Metal nanoparticles (NPs) embedded in carbon materials are very important for various applications, including electrocatalysis. Their catalytic properties are dependent on the intrinsic activity and number of active sites.^{1–8} To add to the quantity of active sites in metal-based electrocatalysts, it is crucial to increase metal loading and dispersity. Most metal NPs are synthesized by injection approaches, yet it is hard to acquire metal NPs of high loading and dispersity.

Due to their uniform composition and morphology,^{9–11} metal–organic frameworks (MOFs) have been regarded as promising precursors for the preparation of carbon-supported well-dispersed metal NPs.^{12–17} However, in a majority of MOFs, the serial metal atoms are inclined to assemble during pyrolysis.¹⁸ There are two universal methods, *i.e.*, “metal-doped isolation” and “heteroatom doping”, that have generally been used to moderate the issue of severe metal agglomeration in the carbonization of MOFs. The metal-doped isolation method employs a second metal that is easily eliminated to enlarge the neighboring distances of the targeted metals.^{19–23} Nevertheless, this method loses the metal density on carbon, which would limit their entire catalytic performance. On the other hand, the “heteroatom doping” method brings in heteroatoms to serve as anchors for the fixing of metal NPs.^{24–29} But the low amount of heteroatoms in the MOFs is not able to prevent a large number of metal NPs from aggregating. To solve

this puzzle, more valid strategies are required to settle the equilibrium between metal density and dispersity for MOF-derived metal NPs embedded in carbon materials.

Here, we design an approach of “vapor adsorption” to restrain metal agglomeration in the calcination of MOFs for the preparation of high-density metal NPs with high dispersion embedded in carbon materials. Considering the high volatility of ferrocene (Fc), the desired Fe(25)@Zn-MOF (mass ratio of Fc to Zn-MOF is 1 : 4) precursor was obtained by vapor adsorption treatment (Zn-MOF and Fc mixture sealed and heated at 150 °C for 24 h). Fc could be uniformly adsorbed on the surface of Zn-MOF *via* this method. Since the radius of an iron atom is smaller than that of a zinc atom, iron migrates to zinc during pyrolysis to obtain Fe NPs and Zn NPs, whose size is smaller than that of Zn NPs, thus achieving the goal of reducing the size of the metal NPs. Moreover, melamine with a high content of N heteroatoms can offer anchoring for metal ions. After calcination at 800 °C, Fe(25)@Zn-MOF was converted to N-doped carbon-supported Fe NPs and Zn NPs (Fe(25)Zn@NC-m) with small-sized metal NPs (7 nm). The resulting Fe(25)Zn@NC-m exhibits excellent electrocatalytic activity in the oxygen reduction reaction (ORR). Moreover, a primary zinc–air battery employing Fe(25)Zn@NC-m as a cathode material achieves a high peak power density of 196 mW cm^{−2}. Experimental results reveal that the good dispersion of small metal NPs with a high density of active sites is conducive to the remarkable ORR performance of Fe(25)Zn@NC-m.

The powder X-ray diffraction (PXRD) pattern of Fe(25)@Zn-MOF reveals characteristic diffraction peaks of Zn-MOF instead of those of Fc (Fig. S1, ESI†). Combined with scanning electron microscopy (SEM), nanorods of Fe(25)@Zn-MOF are more well-stacked than those of Zn-MOF (Fig. 1a) and there are no obvious impurities (Fig. 1b and Fig. S2, ESI†), proving that Fc was adsorbed on the surface of Zn-MOF. Fe(25)@Zn-MOF was then pyrolyzed with melamine to yield Fe NPs and Zn NPs protected by N-doped porous carbon. The morphology of the pyrolyzed sample was further inspected by SEM and transmission electron microscopy (TEM). Fe(25)Zn@NC-m occurs as

State Key Laboratory of Coordination Chemistry, School of Chemistry and Chemical Engineering, Collaborative Innovation Center of Advanced Microstructures, Nanjing University, Nanjing 210023, P. R. China. E-mail: zhenghg@nju.edu.cn

† Electronic supplementary information (ESI) available. See DOI: <https://doi.org/10.1039/d4cc00119b>



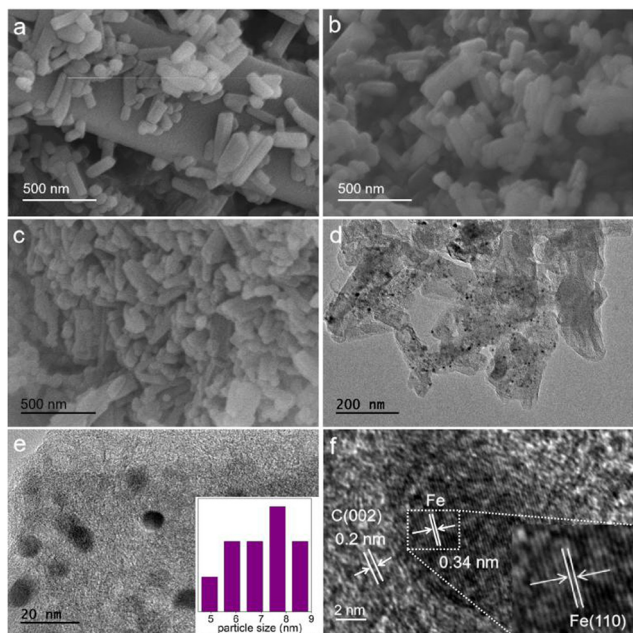


Fig. 1 (a)–(c) SEM images of (a) Zn-MOF, (b) Fe(25)@Zn-MOF, and (c) Fe(25)Zn@NC-m; (d) TEM image, and (e) and (f) HRTEM image of Fe(25)Zn@NC-m.

nanorods keeping the crystal morphology of the precursor (Fig. 1c and d). Ultrasmall metal NPs (7 nm) of high density uniformly embedded in carbon nanorods can be discovered under TEM (Fig. 1d and e). To corroborate the existence of Fe NPs in Fe(25)Zn@NC-m, high-resolution TEM (HRTEM) measurement was carried out. For Fe(25)Zn@NC-m, two apparent lattice stripes of d-spacings 0.20 nm and 0.34 nm, corresponding to Fe (110) and C (002) planes, respectively, were observed in the image (Fig. 1f).³⁰ Scanning TEM (STEM) and elemental mapping images further confirmed the composition of Fe(25)Zn@NC-m, as well as the distribution of C, N, O, Fe and Zn elements (Fig. S3, ESI†).

The absorption-desorption isotherm of Fe(25)Zn@NC-m can be recognized as an obvious hysteresis loop, and the Brunauer-Emmett-Teller (BET) surface area is $459 \text{ m}^2 \text{ g}^{-1}$ (Fig. 2a). The curve of pore size distribution (PSD) indicates the coexistence of micropores, mesopores and macropores (Fig. 2b). In short, the large specific surface area is more conducive to electrolyte and electrode contact, more conducive to the exposure of the active sites, and the large aperture can increase the transmission of charge and mass, which is conducive to improving the electrocatalytic activity. This causes Fe(25)Zn@NC-m with a hierarchical pore structure to show higher catalytic activity. The BET surface area and PSD of Zn@NC-m are similar to those of Fe(25)Zn@NC-m, indicating that the Fe nanoparticles had little effect on both (Fig. S4, ESI†). As shown in Fig. 2c, there is a wide peak located at approximately 26° , which can be assigned to C(002). Additionally, two weak peaks at around 44.7° and 65.0° can be referenced to Fe(110) and Fe(200) (PDF#87-0721).

X-Ray photoelectron spectroscopy (XPS) (Fig. 2d) reveals the existence of C, N, O, Fe, and Zn species in Fe(25)Zn@NC-m. The

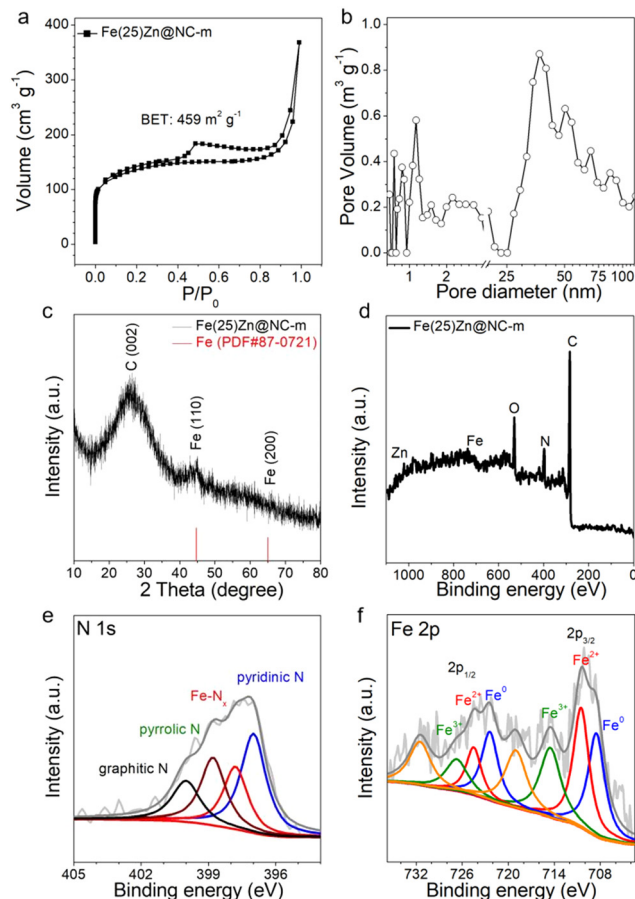


Fig. 2 (a) N_2 absorption-desorption isotherm, (b) pore size distribution, (c) PXRD, (d) XPS survey spectrum, high-resolution (e) N 1s, and (f) Fe 2p XPS spectra of Fe(25)Zn@NC-m.

spectrum of N 1s (Fig. 2e) can be divided into three peaks of pyridinic N (397.0 eV), Fe-N_x (397.7 eV), pyrrolic N (398.8 eV), and graphitic N (400.0 eV). The Fe 2p spectrum (Fig. 2f) shows one obvious peak at around 708.5 eV (Fe $2p_{3/2}$), demonstrating the existence of Fe⁰ in Fe nanoparticles. The distinct peaks at 710.5 eV and 714.5 eV combined with a satellite peak at 719.0 eV are attributed to Fe $2p_{3/2}$ of high valence, which is also proof of Fe-N_x species.³⁰ The N 1s and Fe 2p spectra reveal the successful synthesis of Fe nanoparticles, pyridinic N, Fe-N_x, and graphitic N, which are usually considered to be available sites contributing a lot to ORR activity.³¹

The spectrum of Zn 2p (Fig. S5a, ESI†) can be divided into two peaks of Zn⁰ $2p_{3/2}$ (1022.0 eV) and Zn⁰ $2p_{1/2}$ (1045.0 eV). This indicates that Zn²⁺ is completely reduced to Zn nanoparticles at high temperature. The content of Zn can also be controlled by the pyrolysis temperature. With an increase in temperature, Zn nanoparticles gradually volatilize to produce micropores, which is conducive to the exposure and mass transfer of the active sites.³²

The high-resolution C 1s spectrum can be split into three peaks at 283.5 eV , 285.0 eV , and 286.3 eV , corresponding to C=C/C-C, C-N/C-O and C=N/C=O moieties (Fig. S5b, ESI†).³³ The high-resolution O 1s spectrum (Fig. S5c, ESI†) can be fitted



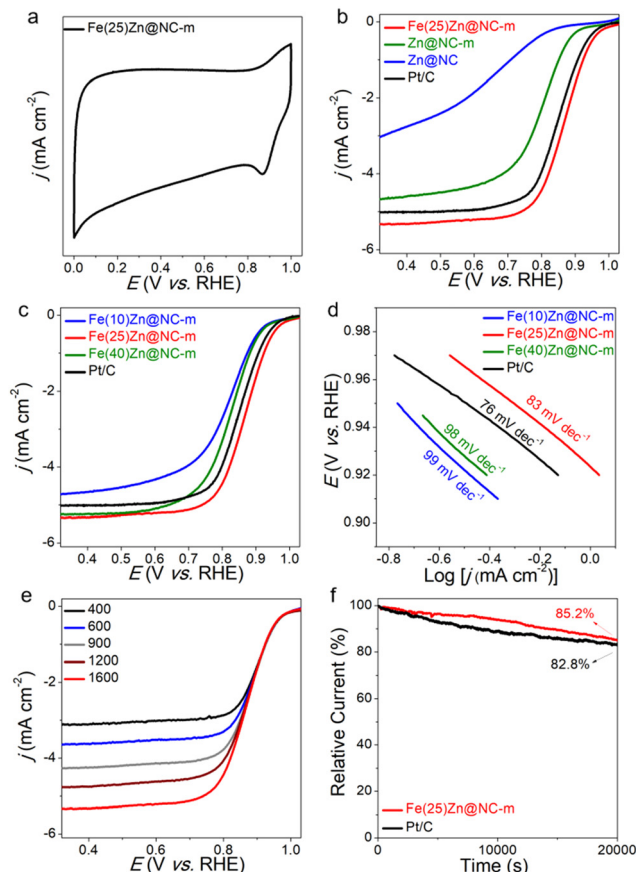


Fig. 3 (a) CV curve of Fe(25)Zn@NC-m. (b) LSV curves of Zn@NC-m, Fe(25)Zn@NC-m, and Pt/C. (c) LSV curves and (d) Tafel plots of Fe(10)Zn@NC-m, Fe(25)Zn@NC-m, and Fe(40)Zn@NC-m. (e) LSV curves of Fe(25)Zn@NC-m at various rotation speeds. (f) chronoamperometric profiles of Fe(25)Zn@NC-m and Pt/C.

to three peaks at 529.8, 531.2, and 532.8 eV, which correspond to O=C, HO-C, and O-C, respectively. C-N and C-O prove that O and N are successfully incorporated into the 3D carbon framework.

We then probed the ORR performance of the as-prepared samples in 0.1 M KOH. The cyclic voltammetry (CV) curve of Fe(25)Zn@NC-m exhibits a positive potential for surface oxide reduction (Fig. 3a). Linear sweep voltammetry (LSV) curves at 1600 rpm have been compared in Fig. 3b. Fe(25)Zn@NC-m exhibits a large half-wave voltage ($E_{1/2}$) of 0.868 V (vs. RHE) and an ultimate current density of 5.4 mA cm^{-2} , which are much higher than those of Zn@NC (0.647 V and 3.1 mA cm^{-2}) or Zn@NC-m (0.795 V and 4.7 mA cm^{-2}). Then, the influence of Fe loading on the ORR activity of Fe/Zn@NC-m samples was researched. The $E_{1/2}$ and limiting current density of Fe(25)Zn@NC-m (Fig. 3c) remain higher than those of Fe(10)Zn@NC-m (0.815 V, 4.73 mA cm^{-2}), Fe(40)Zn@NC-m (0.826 V, 5.22 mA cm^{-2}), or Pt/C (20 wt% Pt) (0.853 V, 5.0 mA cm^{-2}). Encouragingly, the $E_{1/2}$ of Fe(25)Zn@NC-m for ORR can be compared successfully to most previously reported Fe-based electrocatalysts (Table S1, ESI†). The Tafel plot of Fe(25)Zn@NC-m shows 83 mV dec^{-1} , which is smaller than Fe(10)Zn@NC-m (99 mV dec^{-1}) or

Fe(40)Zn@NC-m (98 mV dec^{-1}), proving the faster reaction kinetics of Fe(25)Zn@NC-m (Fig. 3d). Similarly, the LSV curves of Fe(25)Zn@NC-m at different rotational speeds also indicate fast ORR dynamic due to the increasing limiting current density (Fig. 3e). The electron-transfer number (n) was ~ 4.0 from 0.8 to 0.2 V (Fig. S6, ESI†), illustrating that the ORR catalyzed by Fe(25)Zn@NC-m mainly followed the 4e pathway. Impressively, Fe(25)Zn@NC-m also appears to show wonderful durability (Fig. 3f), where the 85.2% reservation of premier current density is observed in Fe(25)Zn@NC-m after continuous 20 000 s, which surpasses Pt/C (82.8%).

Such huge ORR disparities among Zn@NC, Zn@NC-m, Fe(10)Zn@NC-m, Fe(25)Zn@NC-m and Fe(40)Zn@NC-m could be attributed to the size and dispersity of metal NPs. Zn@NC (Fig. S7a, ESI†) and Zn@NC-m (Fig. S7b, ESI†) show large-sized metal NPs with low uniformity. Fe(10)Zn@NC-m (Fig. 4a and c) shows a large size (20 nm) of metal NPs. Because the content of Fe is low, the generated Fe/Zn nanoparticles are also small, and the large-sized particles mainly come from the accumulation of Zn. Besides, Fe(40)Zn@NC-m (Fig. 4b and d) also displays a large size (50–60 nm) of metal NPs. Because of excess iron, this leads to iron aggregation. Thus, the metal particle size of Fe(25)Zn@NC-m is smaller and more evenly dispersed than in the above samples, which proves that the “vapor adsorption” strategy is feasible.

A primary Zn–air battery (Fig. S8a, ESI†) containing Fe(25)Zn@NC-m shows a maximum power density of 196 mW cm^{-2} , above that of commercial Pt/C (144 mW cm^{-2}). The Fe(25)Zn@NC-m-based battery displays a larger specific capacity (620 mA h g^{-1}) than that of Pt/C (503 mA h g^{-1}) at 10 mA cm^{-2} (Fig. S8b, ESI†).

In summary, by using a “vapor adsorption” strategy, uniform carbon-protected small-sized metal NPs with high density have been synthesized successfully. Observably, Fe(25)Zn@NC-m exhibits wonderful ORR activity in 0.1 M KOH. The prominent ORR performance results from the small size of Fe NPs and carbon rods. By and large, this straightforward strategy might be

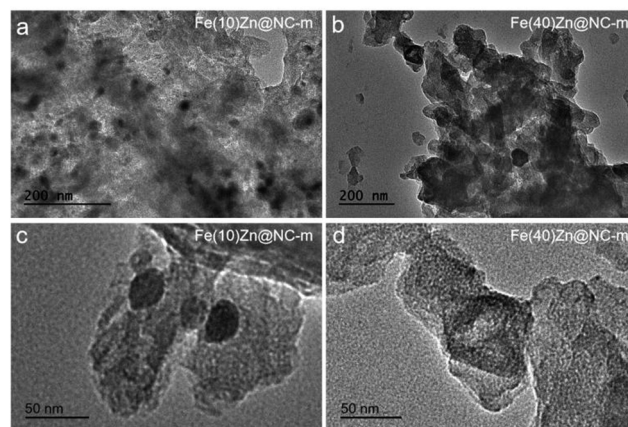


Fig. 4 TEM images of (a) and (c) Fe(10)Zn@NC-m and (b) and (d) Fe(40)Zn@NC-m.



extended to the design of small-sized, high-loading and well-dispersed metal NPs for replacing noble metal catalysts.

This work was supported by the National Natural Science Foundation of China (21771101).

Conflicts of interest

There are no conflicts to declare.

Notes and references

- 1 X. Y. Xie, L. Shang, R. Shi, G. I. N. Waterhouse, J. Q. Zhao and T. R. Zhang, *Nanoscale*, 2020, **12**, 13129–13136.
- 2 M. T. Zhang, H. Li, J. X. Chen, F. X. Ma, L. Zhen, Z. H. Wen and C. Y. Xu, *Adv. Funct. Mater.*, 2023, **33**, 2209726.
- 3 L. X. Wang, L. Wang, X. J. Meng and F. S. Xiao, *Adv. Mater.*, 2019, **31**, 1901905.
- 4 X. Y. Xie, L. S. Peng, H. Z. Yang, G. I. N. Waterhouse, L. Shang and T. R. Zhang, *Adv. Mater.*, 2021, **33**, 2101038.
- 5 F. J. Guo, M. Y. Zhang, S. C. Yi, X. X. Li, R. Xin, M. Yang, B. Liu, H. B. Chen, H. M. Li and Y. J. Liu, *Nano Res. Energy*, 2022, **1**, e9120027.
- 6 Y. C. Wu, W. Wei, R. H. Yu, L. X. Xia, X. F. Hong, J. X. Zhu, J. T. Li, L. Lv, W. Chen and Y. Zhao, *Adv. Funct. Mater.*, 2022, **32**, 2110910.
- 7 S. H. Chen, W. H. Li, W. J. Jiang, J. R. Yang, J. X. Zhu, L. Q. Wang, H. H. Ou, Z. C. Zhuang, M. Z. Chen and X. H. Sun, *Angew. Chem., Int. Ed.*, 2022, **61**, e202114450.
- 8 J. X. Zhu, L. X. Xia, W. X. Yang, R. H. Yu, W. Zhang, W. Luo, Y. H. Dai, W. Wei, L. Zhou, Y. Zhao and L. Q. Mai, *Energy Environ. Mater.*, 2022, **5**, 655–661.
- 9 H. Furukawa, K. E. Cordova, M. O'Keeffe and O. M. Yaghi, *Science*, 2013, **341**, 1230444.
- 10 S. Kitagawa, R. Kitaura and S. I. Noro, *Angew. Chem., Int. Ed.*, 2004, **43**, 2334–2375.
- 11 Y. X. Ye, L. S. Gong, S. C. Xiang, Z. J. Zhang and B. L. Chen, *Adv. Mater.*, 2020, **32**, 1907090.
- 12 H. F. Wang, L. Y. Chen, H. Pang, S. Kaskel and Q. Xu, *Chem. Soc. Rev.*, 2020, **49**, 1414–1448.
- 13 S. Dang, Q. L. Zhu and Q. Xu, *Nat. Rev. Mater.*, 2018, **3**, 17075.
- 14 L. Y. Chen, H. F. Wang, C. X. Li and Q. Xu, *Chem. Sci.*, 2020, **11**, 5369–5403.
- 15 G. R. Cai, P. Yan, L. L. Zhang, H. C. Zhou and H. L. Jiang, *Chem. Rev.*, 2021, **121**, 12278–12326.
- 16 K. Shen, X. D. Chen, J. Y. Chen and Y. W. Li, *ACS Catal.*, 2016, **6**, 5887–5903.
- 17 R. V. Jagadeesh, K. Murugesan, A. S. Alshammari, H. Neumann, M. M. Pohl, J. Radnik and M. Beller, *Science*, 2017, **358**, 326–332.
- 18 C. H. Wang, J. Kim, J. Tang, M. Kim, H. Lim, V. Malgras, J. You, Q. Xu, J. S. Li and Y. Yamauchi, *Chem*, 2020, **6**, 19–40.
- 19 X. P. Han, X. F. Ling, Y. Wang, T. Y. Ma, C. Zhong, W. B. Hu and Y. D. Deng, *Angew. Chem., Int. Ed.*, 2019, **58**, 5359–5364.
- 20 B. Y. Guan, L. Yu and X. W. Lou, *Energy Environ. Sci.*, 2016, **9**, 3092–3096.
- 21 P. Q. Yin, T. Yao, Y. E. Wu, L. R. Zheng, Y. Lin, W. Liu, H. X. Ju, J. F. Zhu, X. Hong and Z. X. Deng, *Angew. Chem., Int. Ed.*, 2016, **55**, 10800–10805.
- 22 Y. Z. Chen, C. M. Wang, Z. Y. Wu, Y. J. Xiong, Q. Xu, S. H. Yu and H. L. Jiang, *Adv. Mater.*, 2015, **27**, 5010–5016.
- 23 R. Wang, X. Y. Dong, J. Du, J. Y. Zhao and S. Q. Zang, *Adv. Mater.*, 2018, **30**, 1703711.
- 24 H. Tabassum, W. H. Guo, W. Meng, A. Mahmood, R. Zhao, Q. F. Wang and R. Q. Zou, *Adv. Energy Mater.*, 2017, **7**, 1601671.
- 25 J. L. Yang, Z. C. Ju, Y. Jiang, Z. Xing, B. J. Xi, J. K. Feng and S. L. Xiong, *Adv. Mater.*, 2018, **30**, 1700104.
- 26 L. Yang, X. F. Zeng, W. C. Wang and D. P. Cao, *Adv. Funct. Mater.*, 2018, **28**, 1704537.
- 27 W. Yao, J. M. Chen, Y. J. Wang, R. Q. Fang, Z. Qin, X. F. Yang, L. Y. Chen and Y. W. Li, *Angew. Chem., Int. Ed.*, 2021, **60**, 23729–23734.
- 28 M. D. Zhang, Q. B. Dai, H. G. Zheng, M. D. Chen and L. M. Dai, *Adv. Mater.*, 2018, **30**, 1705431.
- 29 D. X. Ji, L. Fan, L. Tao, Y. J. Sun, M. G. Li, G. R. Yang, T. Q. Tran, S. Ramakrishna and S. J. Guo, *Angew. Chem., Int. Ed.*, 2019, **58**, 13840–13844.
- 30 X. W. Song, S. Zhang, H. Zhong, Y. Gao, L. A. Estudillo-Wong, N. Alonso-Vante, X. Shu and Y. Feng, *Inorg. Chem. Front.*, 2021, **8**, 109–121.
- 31 J. W. Zhu, H. Zhou, C. T. Zhang, J. Zhang and S. C. Mu, *Nanoscale*, 2017, **9**, 13257–13263.
- 32 X. J. Wang, X. X. Fan, H. H. Lin, H. Fu, T. Wang, J. Zheng and X. G. Li, *RSC Adv.*, 2016, **6**, 37965–37973.
- 33 R. Jiang, L. Li, T. Sheng, G. F. Hu, Y. G. Chen and L. Y. Wang, *J. Am. Chem. Soc.*, 2018, **140**, 11594–11598.

